Journal of Chromatography A 1740 (2025) 465543

Contents lists available at ScienceDirect

Journal of Chromatography A

journal homepage: www.elsevier.com/locate/chroma

Modeling the extra column volume of a micro simulated moving bed chromatography system: Introducing the equivalent radial flow rate distribution

Juliane Diehm, Matthias Franzreb *

Institute of Functional Interfaces, Karlsruhe Institute of Technology, 76344 Eggenstein-Leopoldshafen, Germany

ARTICLE INFO

Keywords:
Chromatography modeling
Extra column volume
Dead volume
Small-scale chromatography
Multi-column chromatography

ABSTRACT

Recently, the focus in chromatography model development has expanded to include the modeling of extra column volume (ECV), particularly in small- and lab-scale systems where ECV can constitute a significant portion of the total volume. Typically, ECV is modeled with 1D approaches, for example with combinations of dispersed plug flow reactors (DPFRs) and continuously stirred tank reactors (CSTRs). However, radial inhomogeneities in the ECV concentration profile necessitate higher-dimensional models for more accurate predictions. Searching for a suitable modeling approach for a micro simulated moving bed chromatography (μSMB) system, we investigated whether the 2D laminar flow model can be extended to account for additional dispersion effects, such as Dean vortices, through an equivalent radial flow rate distribution (eqFRD). For this purpose, we conducted 3D CFD simulations of the respective ECV and adapted the radial flow rate profile of a 2D simulation to match the residence time distribution observed in the CFD results. Applying the eqFRD model led to a significant improvement in prediction accuracy for isolated ECV segments, increasing from 90% to 97% compared to traditional ECV models. However, when these models were applied to the full μSMB system, the choice of ECV model had minimal impact on overall results as long as retention time within the ECV was accurately predicted. This suggests that, in the studied system, the column has a greater influence on peak shape than the ECV, allowing simpler ECV models to suffice in certain contexts. Despite these advances, significant deviations between predicted and experimental results were observed, indicating that factors such as the transition between the column and ECV, as well as detector effects, should be considered in future research. The results underscore the importance of selecting an ECV model in the context of the entire system, balancing accuracy with computational efficiency.

1. Introduction

Chromatography is the predominant method for downstream processing (DSP) of biopharmaceutical products [1]. As product titers increase, the focus of cost reduction shifts from upstream processing to DSP, with chromatography emerging as the main cost driver [2]. This has prompted a considerable effort to optimize chromatography process development and reduce production expenses [1–3].

One effective strategy for cost reduction in preparative applications is the implementation of (continuous) multi-column methods, such as simulated moving bed chromatography (SMB) and periodic counter-current chromatography (PCC) [1]. These techniques offer numerous benefits, including higher capacity utilization, reduced solvent consumption, and increased productivity [1,4]. Simultaneously, the adoption of miniaturization and advanced process modeling aims to minimize experimental efforts and associated costs in process development [3,5]. The use of miniaturized single-column chromatography systems enables material and time efficient determination of important process parameters, often in an automatized fashion [5,6]. These single-column experiments, combined with chromatography modeling, can be sufficient for multi-column process development. Nonetheless, miniaturized multi-column systems can be advantageous: continuous processes reduce the required equipment scale by approximately a factor of ten compared to batch operations, making batch chromatography systems unsuitable for some applications [3]. Kortmann et al. developed a miniaturized PCC system with potential applications in condition screening or product capture from perfusion cell cultures [7]. Recently, we developed a micro SMB (μSMB) system and demonstrated its applicability as a resource-saving tool in small-scale continuous

* Corresponding author.
E-mail address: matthias.franzreb@kit.edu (M. Franzreb).

https://doi.org/10.1016/j.chroma.2024.465543
Received 24 September 2024; Received in revised form 18 November 2024; Accepted 19 November 2024
Available online 26 November 2024

process development [8] as well as for process analytics [9]. The scaled-down equipment significantly conserves resources, especially for long-term studies, while the reduced scale also allows for a fast response time in analytical applications.

Detailed modeling is critical for either performance comparison across scales or optimization of process parameters. While chromatography columns are typically modeled using one-dimensional approaches, such as the general rate model or the equilibrium dispersive model [10,11], different approaches exists for the modeling of the extra column volume (ECV).

SMB is a quasi-continuous binary separation technique that continuously separates a feed stream into two product streams by using multiple interconnected chromatography columns, divided into four zones by inlets and outlets. This results in a different flow rate in each of the zones and through the timed movement of columns, each zone fulfills a specific function, including separation of components and regeneration of the stationary and mobile phases. A detailed explanation of the SMB principle can be found in literature [12–14].

In preparative SMB, accurate modeling is essential for determining optimal process points, ensuring efficient separation, and accounting for ECV. ECV is commonly modeled as either an ideal plug flow reactor (PFR) [15], accounting only for time delay without dispersion effects, or as a dispersed plug flow reactor (DPFR) [16], considering uniform dispersion and time delay.

DPFRs are also frequently used to model capillaries in lab-scale systems, in conjunction with continuously stirred tank reactors (CSTRs) to account for mixing effects in other system components, such as valves and detectors [17–19]. However, the flow rate dependency of model parameters is often seen as a drawback in lab-scale systems. To address this, Baran et al. implemented a two-dimensional DPFR considering the radial laminar flow profile, demonstrating good predictability of ECV behavior across a wide range of flow rates [20]. Filip et al. implemented computational fluid dynamics (CFD) models at various geometric levels, showing that under certain conditions, the most detailed model, which includes curvatures and diameter changes, is necessary to accurately predict ECV effects under all tested conditions [21]. Therefore, a trade-off exists between simple DPFR+CSTR models, which offer short computation times but may be inaccurate if the flow rate deviates significantly from the calibration flow rate, and more sophisticated models, such as CFD models, which provide accurate predictions regardless of flow rate but require much longer computation times. This is particularly important when using small chromatography columns, where ECV significantly influences overall dispersion behavior [22], necessitating a more detailed ECV model.

Thus, in the case of the μSMB system, a significant impact of the ECV on the overall system performance is expected and a detailed ECV model required. However, modeling ECV with CFD is impractical for continuous processes where the same portion of ECV must be modeled multiple times, potentially at different flow rates. Consequently, there is a need for a flow rate-independent, accurate prediction of ECV with low computation time.

Given the considerable differences between state-of-the-art ECV modeling in preparative SMB and miniaturized single-column chromatography, we found a limitation in existing ECV models. To address this, we explored the feasibility of transferring the two-dimensional DPFR approach to other flow rate distributions beyond the laminar flow profile, thereby accounting for all ECV effects. This new approach is termed the equivalent radial flow rate distribution (eqFRD).

In this study, we provide a brief overview of current model approaches and the considerations for establishing the eqFRD. We then compare various ECV modeling approaches in different scenarios, ranging from simple capillaries to the ECV of a μSMB system.

2. Theoretical background

2.1. Overview of common ECV models

Currently, the most common approach for ECV modeling of lab-scale chromatography systems is with CSTRs, (D)PFRs or a combination thereof [17–19]. CSTRs are usually applied for modeling elements with distinct mixing effects like valves and mixers [17]. The change in concentration c of component i over time t can be described according to (1) with the inlet concentration $c_{i,\mathrm{in}}$ and the average residence time τ [23], which is the quotient of the CSTR's volume V_{CSTR} and the volumetric flow rate q [24]. PFRs, on the other hand, add a lag time caused by delay volume and are used for the modeling of capillaries [17]. While ideal PFRs solely consider mass transfer by convection, DPFRs have an additional term to include dispersion effects. DPFRs can be described using (2) with the mean linear velocity u_0, spatial coordinate z and the dispersion coefficient D_{ECV} [16]. If D_{ECV} is set to zero, the resulting equation describes a PFR; due to the spatial discretization in the simulation process, leading to so called numerical dispersion, the resulting model still will have a dispersion greater than zero. This effect can be utilized to obtain an accurate model with a low number of spatial grid-points, thus increasing the numerical efficiency. The required number of grid-points N_{ECV} can be approximated with (3) [16], with the length of the ECV L_{ECV} [16]; with only one grid-point, the model equals a CSTR model and with infinite grid-points it is a PFR model.

$$\frac{\delta c_i}{\delta t} = \frac{c_{i,\mathrm{in}} - c_i}{\tau} \tag{1}$$

$$\frac{\delta c_i}{\delta t} + u_0 \frac{\delta c_i}{\delta z} = D_{\mathrm{ECV}} \frac{\delta^2 c_i}{\delta z^2} \tag{2}$$

$$N_{\mathrm{ECV}} = \frac{L_{\mathrm{ECV}} u_0}{2 D_{\mathrm{ECV}}} \tag{3}$$

For certain flow patterns and conditions, D_{ECV} can be calculated. For example, in a straight capillary with laminar flow, it can be calculated using (4) with the molecular diffusion coefficient D_{m}, the radius of the capillary R and the coefficient $\kappa = 48$ (for laminar flow in a straight tube), if the conditions of Taylor–Aris dispersion are fulfilled [25,26]. This can be verified with (5), which tests if the residence time in the capillary is long enough to reach a radial concentration equilibrium and can thus be treated as a DPFR [20,25].

$$D_{\mathrm{ECV}} = D_{\mathrm{m}} + \frac{u_0^2 R^2}{\kappa D_{\mathrm{m}}} \tag{4}$$

$$L_{\mathrm{crit}} > \frac{u_0 R^2}{4 D_{\mathrm{m}}} \tag{5}$$

If condition (5) is not met, the radial flow distribution of the laminar flow profile leads to so called peak splitting, where the convection peak consisting of molecules close to the center of the capillary moves faster compared to the diffusion peak at the perimeters of the capillary. This effect is particularly pronounced for macro molecules due to their lower molecular diffusion coefficient and has already been extensively discussed [20,27]. To account for this effect, the radial flow profiles as well as radial diffusion have to be considered in (2) [20]:

$$\frac{\delta c_i}{\delta t} + u(r) \frac{\delta c_i}{\delta z} = D_{\mathrm{m}} \frac{1}{r} \frac{\delta}{\delta r} \left(\frac{\delta c_i}{\delta r} r \right) + D_{\mathrm{m}} \frac{\delta^2 c_i}{\delta z^2} \tag{6}$$

with the radial flow distribution $u(r)$ according to (7) in case of laminar flow [20].

$$u(r) = 2 u_0 \left[1 - \left(\frac{r}{R} \right)^2 \right] \tag{7}$$

Alongside the temporal dimension, the partial differential equation for describing mass transport in the ECV now has two spatial dimensions, z and r. In real systems, additional effects often occur that are not captured by (7), an example are so-called Dean vortices, which can arise in curved capillaries due to centrifugal forces and cause further

dispersion [28]. These effects can be modeled, for instance, by 3D CFD models [21]. Whether Dean vortices need to be considered can be determined with the Dean number Dn calculated using (8) with the Reynolds number Re, the capillary diameter d, the curvature radius R_c, the fluid density ρ, the dynamic viscosity η, and the Schmidt number Sc; if condition (10) is met, the centrifugal forces can be neglected [21].

$$Dn = Re\sqrt{\frac{d}{2R_c}} \tag{8}$$

$$Re = \frac{\rho u_0 d}{\eta} \tag{9}$$

$$Dn^2 Sc < 100 \tag{10}$$

$$Sc = \frac{\eta}{\rho D_m} \tag{11}$$

Filip et al. used 3D CFD simulations for geometries where the Dean vortices could not be neglected [21]. However, CFD simulations are so far only applied in the context of single-column chromatography, as the computation time is often too long for multi-column chromatography, especially when continuous multi-column chromatography experiments are to be simulated over a long period.

2.2. Equivalent radial flow rate distribution

Currently, there is a notable gap in modeling ECV when condition (5) is not met, meaning the ECV cannot be described with a combination of DPFRs and CSTRs, and effects like Dean vortices prevent the application of (6). This gap is especially evident when the overall system and its application are too complex to model using 3D CFD.

In this work, we tested two different approaches to overcome this issue. In the first approach, we used two DPFRs+CSTRs in parallel to be able to account for radial inhomogeneities in the concentration profile. This approach is quite common when modeling parts with larger volumes that can also exhibit some back-mixing, like mixing chambers [29] or membrane chromatography housings [23], but is usually not applied to other system components. In the second approach, we aimed to reduce the dimensionality required to describe the fluidic effects from 3D to 2D by adjusting the applied flow rate profile and using it in combination with (6). As it is not trivial to experimentally measure the ECV effects for single components like short capillaries or microfluidic channels, we used CFD simulations for the determination of the equivalent flow rate profile. To explain the exact procedure for this approach in more detail, we first examine the radial flow rate distribution in case of laminar flow. For the numerical implementation of (6), the modeled geometry is usually radially discretized in a number n_{rad} of radial cells. If the discretization is done equidistantly, each radial element k will have the area $A(k)$ according to (12). Additionally, a certain percentage of the overall flow q_0, named the flow rate distribution $FRD(k)$, will pass through each radial element according to (13), where the mean linear velocity in the radial element $u(k)$ can be approximated using (7), resulting in (14).

$$A(k) = \pi\left[\left(r(k) + \frac{R}{n_{rad}}\right)^2 - r(k)^2\right] \tag{12}$$

$$FRD(k) = \frac{u(k)\,A(k)}{q_0} \tag{13}$$

$$FRD(k) = \frac{1}{q_0} 2u_0\pi\left[1 - \left(\frac{r(k) + 0.5\frac{R}{n_{rad}}}{R}\right)^2\right]\left[\left(r(k) + \frac{R}{n_{rad}}\right)^2 - r(k)^2\right] \tag{14}$$

If the exact flow profile is unknown, an equivalent radial flow rate distribution ($FRD^*(k)$) can be calculated using a breakthrough curve determined experimentally or through CFD simulation. In many cases, FRD^* does not represent the physical FRD in the respective system but

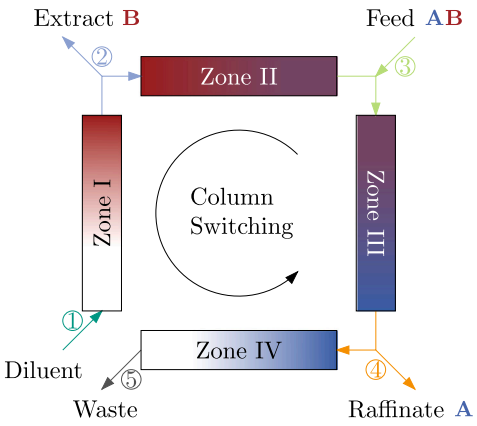

Fig. 1. Schematic of a four column open-loop SMB system with ECV segments 1–5 between the different zones.

leads to a similar outlet concentration profile. Regardless of the actual geometry of the ECV, which can be quite complex, FRD^* is always approximated with a cylindrical geometry, where diameter and length are chosen to match the physical ECV as closely as possible. Eqs. (15)–(17) show the procedure for calculating FRD^* in an iterative process: Without loss of generality, it is assumed that the mean retention time of each radial cell $t_m(k)$ increases with increasing radius (similar to the laminar flow profile). With the iteratively determined maximum retention time in each radial cell $t_{end}(k)$, $t_m(k)$ can be calculated using (15). A concentration threshold for the starting point of the breakthrough curve is set (e.g., $c_{out}(t_{end}(0)) \geq 10^{-10}$ mM) for the calculation of $t_m(1)$. $t_m(k)$ can be used to calculate $FRD^*(k)$ with (16), which is then used to calculate the outlet concentration $c_{out,cal}$ with (17), which is compared to the actual measured (or CFD calculated) outlet concentration $c_{out}(t_{end}(k))$. If (17) is not fulfilled, $t_{end}(k)$ is increased according to the temporal discretization until the smallest possible $t_{end}(k)$ to fulfill (17) is identified. This process is repeated for all radial cells.

$$t_m(k) = t_{end}(k-1) + 0.5\left(t_{end}(k) - t_{end}(k-1)\right) \tag{15}$$

$$FRD^*(k) = \frac{A(k)L_{ECV}}{q_0 t_m(k)} \tag{16}$$

$$c_{out,cal} = \sum_{n=1}^{k} FRD^*(n)c_{in} \leq c_{out}(t_{end}(k)) \tag{17}$$

3. Methods

In this study, various ECV geometries were modeled with different approaches, aiming to accurately represent the ECV of a μSMB system. Even simple test geometries, such as capillaries, were derived from the μSMB's ECV. The μSMB system is an open-loop four-zone system, as depicted in Fig. 1. In previous studies, this system was used with one size-exclusion chromatography column per zone for continuous desalting of proteins [8,9]. The μSMB functionality is realized through a 3D printed central rotary valve, previously described along with the general setup of the μSMB system [8,30]. The chromatography columns of the system divide the ECV into five distinct segments, as shown in Fig. 1. Each segment includes the static part of the valve system, the rotating part of the valve system, and capillaries connecting the chromatography columns to the valve. Exemplary, the ECV segment between zones two and three (segment 3) is depicted in Fig. 2(a). Each segment is further divided into several subsegments based on geometric features, six in the case of Fig. 2(a).

The ECV features diameter changes, curves, and merges (feed) and splits (raffinate/extract). A detailed overview of all dimensions of the

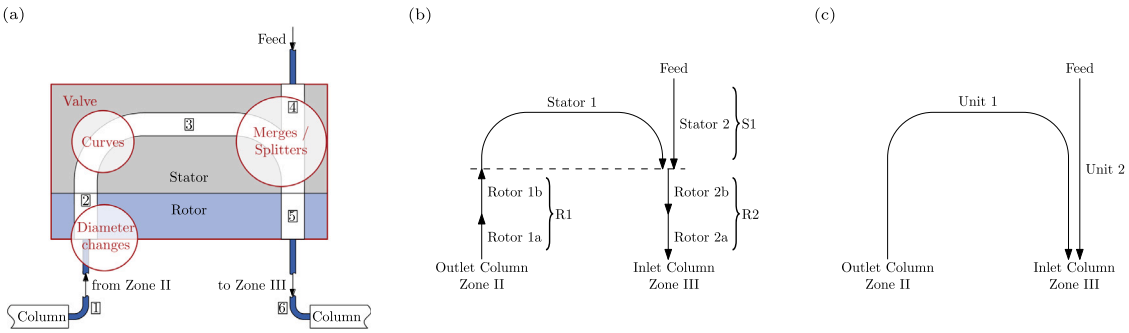

Fig. 2. Overview of modeled geometries: (a) segment of the μSMB ECV between zones two and three, having distinct geometric properties, such as diameter changes, curves and merges. In accordance with the geometric features, this segment of the ECV was further divided into six subsegments. (b) and (c): different modeling approaches for models with fitted parameters. Either, each of the geometric subsegments is represented by one unit in the model (b), or all subsegment along a flow path are combined in one single unit (c).

Table 1
Overview of different modeling approaches of extra column volume with required model parameters and recommended applications. No superscript: geometric/physical parameter, ^{a} calculated parameter, ^{b} fitted with genetic algorithm to calibration experiment, ^{c} calculated based on calibration experiment.

Model	Dimension	Parameters	Applications
PFR	1D	L, d	low ratio of ECV dispersion to column dispersion
DPFR	1D	L, d, D^a_{ECV}	laminar flow with (5) fulfilled
(D)PFR+CSTR	1D	$L^b, d, (D^b_{ECV}), V^b_{CSTR}$	geometries with additional dispersion and (5) fulfilled
parallel (D)PFR+CSTR	1D	$L^b_1, d_1, (D^b_{ECV,1}), V^b_{CSTR,1}, L^b_2, d_2, (D^b_{ECV,2}), V^b_{CSTR,2}, s^b$	geometries with additional dispersion and (5) not fulfilled
laminar	2D	$L, d, D_m, u^a(r)$	laminar flow with (5) not fufilled
eqFRD	2D	$L, d, u^c(r)$	geometries with additional dispersion and (5) not fulfilled under various flow conditions
CFD	2D/3D	L, d, D_m	complex geometries with high accuracy requirements

individual ECV subsegments of the entire μSMB system is provided in Table S1 in the supplementary information (SI). A technical drawing of the 3D printed stator channel is depicted in Fig. S1.

The ECV was modeled using two methods: a unit-by-unit approach, where each subsegment of the ECV was modeled separately, as shown in Fig. 2(b), and a flow path approach, where all subsegments connecting zone two and zone three and all subsegments connecting the feed and zone three were modeled as a single unit, depicted in Fig. 2(c). Before modeling the entire ECV segments, subsegments 1 and 3 were modeled independently to study the effects of Taylor–Aris dispersion and Dean vortices in greater detail.

A complete SMB process was modeled, and the simulation results were compared to previously published experimental data [8]. The applied zone flow rates and other process parameters are detailed in Table S2 in the SI. The column model, including all parameters, was also previously published. The columns were modeled using the 1D general rate model (GRM), assuming no radial concentration profile within the columns, thereby neglecting any influence of the columns' outlet profiles on the ECV behavior. Effects caused by frits etc., were not considered separately but were included in the column model. An detailed overview of the units required for SMB modeling with the different approaches is given in Fig. S2. Similar to the experiments, all simulations were performed for bovine serum albumin (BSA) (D_m = 6.78e–11 m^2/s, calculated according to [31]) and ammonium sulfate (AS) (D_m = 1.2e–9 m^2/s [32,33]). The significant size difference between these molecules is advantageous for investigating ECV effects, as molecular size has been reported to play an important role [20].

Seven different approaches for ECV modeling were evaluated, summarized in Table 1. In this work, the approaches are categorized into models where all parameters can be calculated based on geometric/literature data (PFR, DPFR, laminar, and CFD) and models requiring a calibration experiment (or CFD simulation) for parameter fitting (DPFR+CSTR, parallel DPFR+CSTR) or parameter calculation (eqFRD). Detailed descriptions of these modeling approaches are provided in the following sections.

3.1. CFD models

CFD simulations were performed as a benchmark for the other modeling approaches and also for model calibration (if required). The simulations were conducted using COMSOL Multiphysics version 6.1 (Comsol Multiphysics GmbH, Göttingen, DE), employing the laminar flow and the transport of diluted species physics.

The channels of the valve system (subsegments 2–5 in Fig. 2(a)) were modeled in 3D. The capillaries connecting the columns and the valve system (subsegments 1 and 6) were simplified to straight, unbent capillaries, as the real bending radius is to large for the occurrence of Dean vortices and this assumption reduces computational time significantly. Single capillaries were modeled in 2D. All mesh configurations are listed in Table S3 in the SI.

Simulations were conducted for both pulse injections and breakthrough curves. The exact inlet profiles are provided in the SI (Table S4). The maximum inlet concentration for both cases was 0.03 mol/m^3. Subsegments 1 and 3 were modeled at flow rates of 1, 10, 100, and 1000 µL/min, while the entire ECV segments were modeled at the respective flow rates of the comparable μSMB experiments.

3.2. 1D models

All 1D simulations were performed using the Chromatography Analysis and Design Toolkit (CADET, Institute of Bio- and Geosciences 1 (IBG-1) of Forschungszentrum Jülich (FZJ), Jülich, DE) [34]. PFRs were modeled using the lumped rate model without pores, setting the column porosity to 1 and the column dispersion to 0 m^2/s. For DPFR models, the column dispersion was calculated using (4).

A subsequent CSTR model was added to each DPFR for DPFR+CSTR models. The length of the DPFR L, the dispersion coefficient of the DPFR D_{ECV}, and the volume of the CSTR V_{CSTR} were determined through parameter fitting, with a defined diameter. If only a single subsegment was modeled, the actual diameter was used; otherwise, the diameter of the valve system was chosen. The parameter fitting was performed using the differential evolution algorithm of scipy.optimize. The same time steps were used for both the CFD simulation and the parameter fitting. The mean square error between the outlet concentration of the CFD ($c_{\mathrm{CFD}}(t)$) and the respective simulation ($c_{\mathrm{sim}}(t)$) was chosen as the optimization function y according to (18). When fitting the parameters of a series of DPFR+CSTR units, the parameters of the first unit were fitted initially, followed by fitting the parameters of the subsequent units, including all previous units in series. For fitting parameters of one unit at varying flow rates, the optimization function was modified to sum the mean square errors of all flow rates. For modeling the entire ECV segment as shown in Fig. 2(b), the units Rotor 1a and 1b (as well as 2a and 2b) were combined.

$$y = \sum_{t=0}^{t_{\mathrm{end}}} \left(c_{\mathrm{CFD}}(t) - c_{\mathrm{sim}}(t)\right)^2 \tag{18}$$

The approach for the parallel DPFR+CSTR (P DPFR+CSTR) was similar, except that the volumetric flow rate in each subsegment was divided into two partial flows and modeled separately. The flow rate division ratio s was also determined through parameter fitting. When modeling multiple units in series, the flow rate division ratio remained constant for all units according to the parameter fit of the first unit, resulting in two completely independent flow paths for the entire ECV segment.

3.3. 2D models

2D models were also implemented in CADET, using the 2D GRM reduced to a 2D lumped rate model without pores by setting the column porosity to one. Unless otherwise stated, an equidistant radial discretization with 50 radial cells was applied. For laminar modeling, the actual diameter and length of the respective geometry were used, along with the molecular diffusion coefficient for radial and axial dispersion. The mean linear velocity of each radial cell was calculated using (7).

The eqFRD approach was implemented using a similar 2D GRM in CADET, but the axial and radial dispersion coefficients were set to zero, as molecular diffusion effects were already considered in the parameter calculation based on the CFD simulation results. The radial flow profile FRD^* was calculated based on (16).

Equidistant radial discretization was chosen for modeling single units. For modeling a series of different units, the flow in each radial cell was kept constant to prevent artificial simulated mixing effects. Thus, for a series of units, FRD^* was only calculated for the first unit and kept constant for all subsequent units in series. Instead of changing FRD^*, the specific retention time in each subsequent radial subsegment was adjusted using custom radial discretization, with the area of each radial cell calculated similarly to FRD^*.

When modeling an entire ECV segment, subsegments Rotor 1a and 1b (as shown in Fig. 2(b)) were modeled using the laminar approach, while Rotor 2a and 2b were modeled as a single unit with eqFRD.

4. Results and discussion

4.1. Modeling of straight capillaries

At first, the different model approaches were compared for a straight capillary at varying flow rates. The eqFRD approach was not included, as it equals the laminar approach in case of a straight capillary with laminar flow conditions. Although similar studies have already been conducted [20], we include this for completeness and clarity. The modeled capillary corresponds to subsegments 1 and 6 in Fig. 2(a), representing the capillaries connecting the chromatography columns to the valve system in the μSMB setup. In total, there are eight such capillaries in the μSMB setup, with one at each column's inlet and outlet. The fluidic effects in the capillaries were assumed to be independent of those occurring in the rest of the system for this analysis. The critical flow rate for Taylor–Aris dispersion in this capillary, according to (5), is < 5.6 µL/min for BSA and < 99.5 µL/min for AS. Given that the μSMB system operates between 48 µL/min and 113 µL/min for the considered process, dispersed plug flow behavior cannot be assumed for BSA. Therefore, we investigated the effects of flow rate on the outlet profile.

Fig. 3(a) displays the outlet profiles from CFD simulations of pulse injections of BSA and AS at flow rates ranging from 1 to 1000 µL/min. The vertical black line indicates the volume of the capillary. At flow rates below the critical flow rate, the outlet profiles are nearly symmetrical Gaussian peaks with the expected retention volume. Peak height decreases with lower flow rates due to longer residence times, which enhance axial dispersion effects. At higher flow rates, peak splitting caused by the laminar flow profile is observable: Without sufficient residence time, radial diffusion equilibrium is not achieved, resulting in a faster elution of the molecules at the center of the laminar flow profile in contrast to the molecules close to the wall, causing a strong tailing effect. This effect is more distinctive for BSA, where the peak splitting starts at a flow rate of 10 µL/min, whereas for AS, the effect begins at 100 µL/min, due to the smaller molecular diffusion coefficient of BSA. The peak height increases again at 1000 µL/min because the pulse length had to be increased for numerical stability (8.33 µL for 1000 µL/min compared to 0.83 µL for other flow rates).

Figs. 3(b) and 3(c) depict the breakthrough curves of BSA modeled with different approaches at the flow rates of 1 µL/min and 100 µL/min, respectively. At 1 µL/min, all models except PFR accurately predict the shape of the breakthrough curve in regard to the CFD model. The PFR model exhibits slight dispersion effects due to numerical dispersion. At 100 µL/min, above the critical flow rate, the differences between models become more pronounced. For instance, a DPFR with the dispersion coefficient calculated from (4) is unsuitable. Using a DPFR+CSTR combination with fitted parameters improves results but

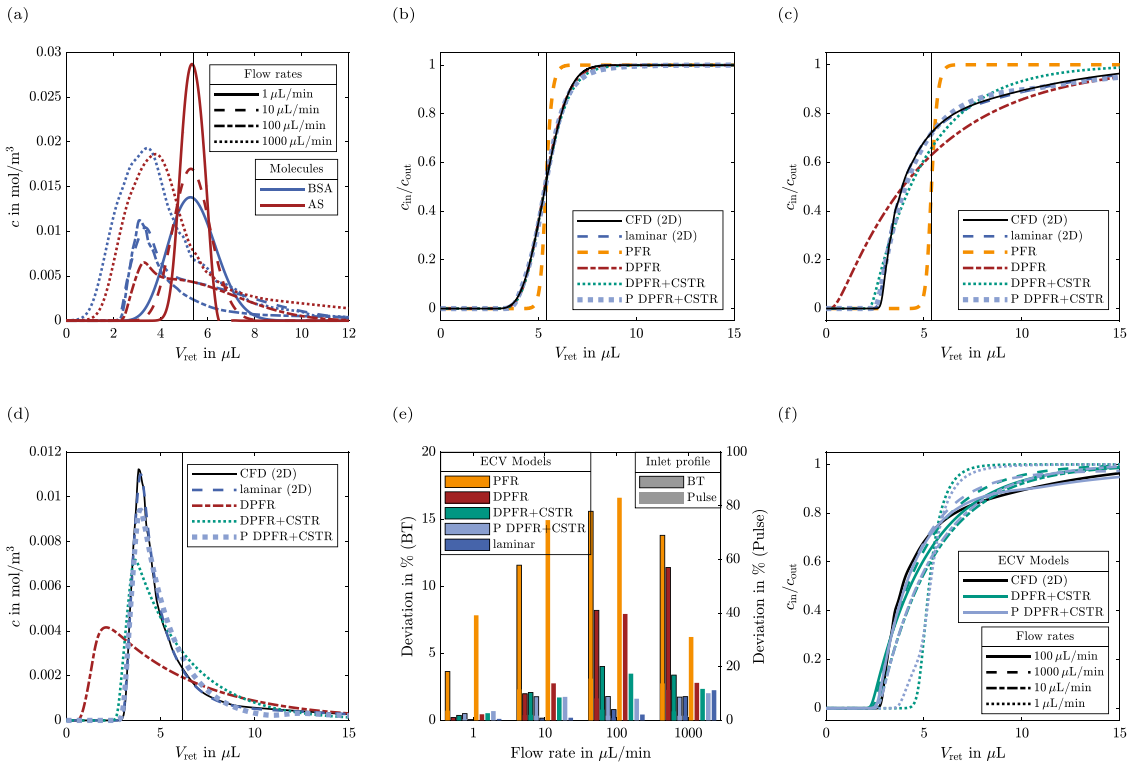

Fig. 3. Modeling of a straight capillary with a length of 0.11 m and a diameter of 0.25e−3 m with varying flow rates and different ECV model approaches. The vertical black lines represent the volume of the capillary. (a): CFD simulations of a pulse injection at different flow rates for BSA and AS. The injection volume at 1000 µL/min is 8.33 µL and 0.83 µL for all other flow rates. (b), (c): Breakthrough curve of BSA at a flow rate of 1 µL/min (b) and 100 µL/min (c) for different modeling approaches. (d): Pulse injection of BSA at a flow rate of 100 µL/min for different modeling approaches. (e): Deviations of different model approaches from the CFD model for breakthrough and pulse injections of BSA. All values were normalized with the total area of the outlet profile of the CFD simulation. (f): Transfer of fitted ECV models (DPFR+CSTR, P DPFR+CSTR) with parameters (L, D_{ECV}, s) fitted at various flow rates to a flow rate of 100 µL/min.

still fails to accurately model the breakthrough curve shape. This can only be achieved using a model that allows for radial discretization, accounting for the peak splitting. Two approaches were considered: the parallel DPFR+CSTR, essentially a 2D DPFR+CSTR with two radial cells, and the laminar model. Due to the low number of radial cells, the parallel DPFR+CSTR was still considered as a 1D approach in this work. Of course, it would be possible to increase the number of parallel DPFR+CSTR units, but for the peak splitting, two cells (one for each peak) are sufficient. While this presents a straight forward model approach, parameter fitting is more complex due to the increased number of parameters, and suitable model parameters for all flow rates could not always be obtained (compare SI Fig. S3). As previously reported, the laminar approach resulted in comparable results to the CFD simulation, even with a low number of radial cells (10 for BSA and 5 for AS, see SI Fig. S4), suggesting it should be used more frequently for ECV modeling.

The same models were applied to pulse injections to assess the versatility of the different approaches. Parameters determined from breakthrough curves were used for models requiring parameter fitting (DPFR+CSTR, P DPFR+CSTR). The laminar model again produced results comparable to the CFD model, while the parallel DPFR+CSTR underestimated peak height but predicted the curve shape correctly. This indicates that models not requiring parameter fitting are more robust under varying experimental conditions.

Fig. 3(e) summarizes the deviations between the tested ECV simulations and the CFD simulation across different flow rates and injection profiles. All outlet profiles and comparable results for AS are included in the SI (Figs. S3, S5, and S6). Deviations were normalized with the overall peak area of the CFD outlet profile for better comparability.

Initially, deviations increase with increasing flow rate and stagnate starting from 100 µL/min for most models. Especially at low flow rates, the laminar model shows the smallest deviations as both the laminar and CFD models consider the radial flow rate profile along with axial and radial diffusion. Among the other models, DPFR performs best at flow rates below q_{crit} but becomes less accurate at higher flow rates. Particularly at higher flow rates, the parallel DPFR+CSTR approach outperforms the DPFR+CSTR. Deviations of the peak injection inlet profile are generally higher than those of the breakthrough curves, likely due to the higher peak area of the breakthrough combined with normalization. In summary, these results illustrate that DPFR with D_{ECV} calculated according to (4) is a valid option for flow rates below q_{crit}, while 2D models are universally applicable under varying conditions, even with a low number of radial cells.

To emphasize this further, Fig. 3(f) shows the application of model parameters fitted at different flow rates for simulations performed at 100 µL/min. The deviation from the CFD model increases with the difference between the fitting and simulation flow rates. While this can sometimes be improved by fitting parameters at multiple flow rates, it remains challenging when different fluidic phenomena dominate at different flow rates. On the other hand, for the not-fitted models, the flow rate is used to calculate the model parameters and thus always considered automatically.

4.2. Modeling of a curved channel

Next, we focused on modeling the curved structure of the valve's stator (subsegment 3 in Fig. 2(a), without merges or splits) at flow rates ranging from 1 to 1000 µL/min. Due to the presence of Dean vortices, the eqFRD approach differs from the laminar approach and both were considered. Table 2 provides an overview at which flow rate the criteria for Taylor–Aris dispersion and Dean vortices are met. Dean

Table 2
Overview of flow conditions. At a flow rate of 1000 µL/min, non of the conditions are met for neither molecule. * condition is met.

		1 µL/min	10 µL/min	100 µL/min
BSA	q_{crit} in µL/min	0.74	0.74	0.74
	Dn^2Sc	2.07*	206.85	20 685.48
AS	q_{crit} in µL/min	13.10*	13.10	13.10
	Dn^2Sc	0.12*	11.69*	1168.73

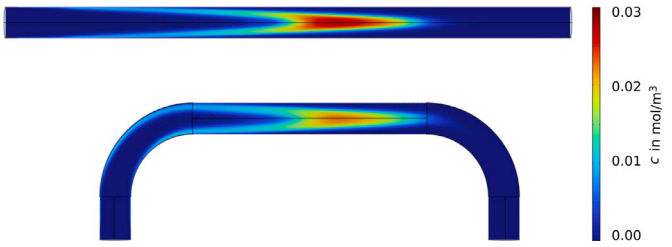

Fig. 4. CFD calculated concentration profile in a longitudinal section of a straight and curved channel. Except for the geometry, conditions are identical in both cases (pulse injection of BSA, 1.5 s after injection, flow rate of 100 µL/min).

vortices significantly increase dispersion compared to laminar flow, as illustrated in Fig. 4, which compares concentration profiles in the center of a longitudinal section of straight and curved channels under identical conditions (L, d, q, D_m).

Fig. 5(a) shows CFD simulations of breakthrough curves for BSA and AS at various flow rates. At low flow rates, the breakthrough curves of BSA are broader than those of AS and the width increases with increasing flow rate. Notably, from a flow rate of 10 µL/min for BSA and 100 µL/min for AS, the curves exhibit a similar shape regardless of flow rate or molecule. Additionally, BSA at 1 µL/min and AS at 10 µL/min display comparable breakthrough curves. These observations are in agreement with Table 2 and indicate that flow conditions for Taylor–Aris dispersion and Dean vortices have a greater impact on the outlet profile than molecular diffusion.

Fig. 5(b) shows the breakthrough curves of BSA at 100 µL/min with different ECV modeling approaches. The DPFR model deviates significantly from the CFD model, as the residence time is too short for Taylor–Aris dispersion to occur. The laminar model illustrates the outlet profile of a straight channel without Dean vortices, characterized by early breakthrough of molecules near the center and tailing of those near the wall. In the curved capillary, these effects are mitigated by additional dispersion caused by Dean vortices. Other ECV models accurately predict the outlet profile.

Fig. 5(c) compares deviations between ECV models and the CFD model across different flow rates and injection profiles for BSA. The outlet profiles for all conditions as well as the comparable results for AS are included in the SI (Figs. S7–S9). Similar to the straight capillary, the deviation increases with flow rate and plateaus at 100 µL/min. Again, deviations for pulse injections are generally higher than those for breakthrough curves and slightly higher than those for the straight capillary but remain below 5% for most breakthrough curves. The eqFRD approach is the most accurate across most flow rates, making it a suitable alternative to the laminar approach when multiple fluidic effects are present. However, achieving high accuracy requires 50 radial cells (see Fig. S10), consequently there is a trade-off between computational time and precision in this case. The increased number of required radial cells likely results from the larger radius compared to the straight capillary rather than the modeling approach itself, as the laminar approach required an increased number as well (see Fig. S11). Unlike the other models, the eqFRD model shows increasing deviations at 1000 µL/min compared to 100 µL/min. This is most likely due to the time discretization used in the simulation as well as the calculation of FRD^*. A time increment of 0.025 s was used across all flow rates, although the total simulation time varied significantly. Consequently, only 36 time steps were required for the breakthrough at a flow rate of 1000 µL/min, compared to 360 and 3600 time steps at flow rates of 100 and 10 µL/min, respectively. Because the precision of the calculated FRD^* is directly linked to the concentration change occurring within each time increment (compare (15)–(17)), the accuracy at higher flow rates can be improved by reducing the time increment.

Similar to Fig. 3(f), Fig. 5(d) shows the transfer of model parameters fitted at various flow rates to simulations performed at 100 µL/min. It is possible to predict the breakthrough curve at 100 µL/min using parameters determined at 1000 µL/min for all methods. However, parameters fitted at 10 µL/min for the DPFR+CSTR model and 1 µL/min for both the DPFR+CSTR and the parallel approach underestimate dispersion effects, resulting in a steeper predicted breakthrough curve. This is because Dean vortices only appear at flow rates above 10 µL/min, with 10 µL/min being at the transition zone. Consequently, these models cannot extrapolate to conditions different from the original flow conditions. In contrast, the eqFRD approach can predict the basic shape of the breakthrough curve even using parameters calculated at 1 µL/min, though deviations from the CFD model increase with the difference between the actual flow rate and the one used for parameter calculation. This demonstrates eqFRD's versatility across various application scenarios, especially when simulating different flow rates over a broad range.

Figs. 5(e) and 5(f) compare the eqFRD at different flow rates for the curved channel and an equivalent straight one (with otherwise the same dimensions) for BSA and AS, respectively. For better comparability between the different flow rates, the equivalent volume (eqV), which is FRD^* normalized with the mean retention time, is depicted instead of FRD^*. An ideal PFR and laminar flow are also included. BSA exhibits nearly ideal laminar flow at high flow rates, with almost no radial diffusion. At lower flow rates, the differences between radial cells decrease, and the profile approaches that of a PFR. This is particularly evident for AS at 1 µL/min, the only condition meeting the criterion for Taylor–Aris dispersion. The remaining deviations from the ideal PFR, leading to peak broadening effects, visualize the dispersion. No difference is observable between the straight and curved channels at low flow rates, which aligns with Table 2. Interestingly, once a deviation between curved and straight channels occurs, all curved channels exhibit the same eqV, independent of flow rate and molecule. This indicates that Dean vortex-induced dispersion outweighs over molecular diffusion effects. The eqV curves for BSA are more consistent compared to AS, explaining the better transferability of calculated FRD^* across different flow rates. For AS, the transfer results in higher deviations (see Fig. S9b), hence, whether the eqFRD can be generalized over a broad flow rate range needs to be verified for each scenario.

Overall, the new eqFRD approach offers a valuable alternative to 2D simulations with a laminar flow profile, particularly when multiple effects occur simultaneously. It provides a reliable method for various simulation conditions, especially for larger molecules. When strong dispersion effects are present, simpler approaches like DPFRs can also be sufficient. The optimal modeling approach should be determined based on the specific application, balancing modeling accuracy and computational time.

4.3. Combination of different subsegments

After analyzing different subsegments of the ECV individually, we proceeded to model entire segments using the different approaches. It is known that dispersion effects occurring in ECV are not additive, nonetheless additive behavior is often assumed for simplification [35, 36]. Here, we investigated whether it is acceptable to assume additive behavior and determine the model parameters of each subsegment independently, or if all subsegments need to be considered together during model development. The results are shown in Fig. 6(a).

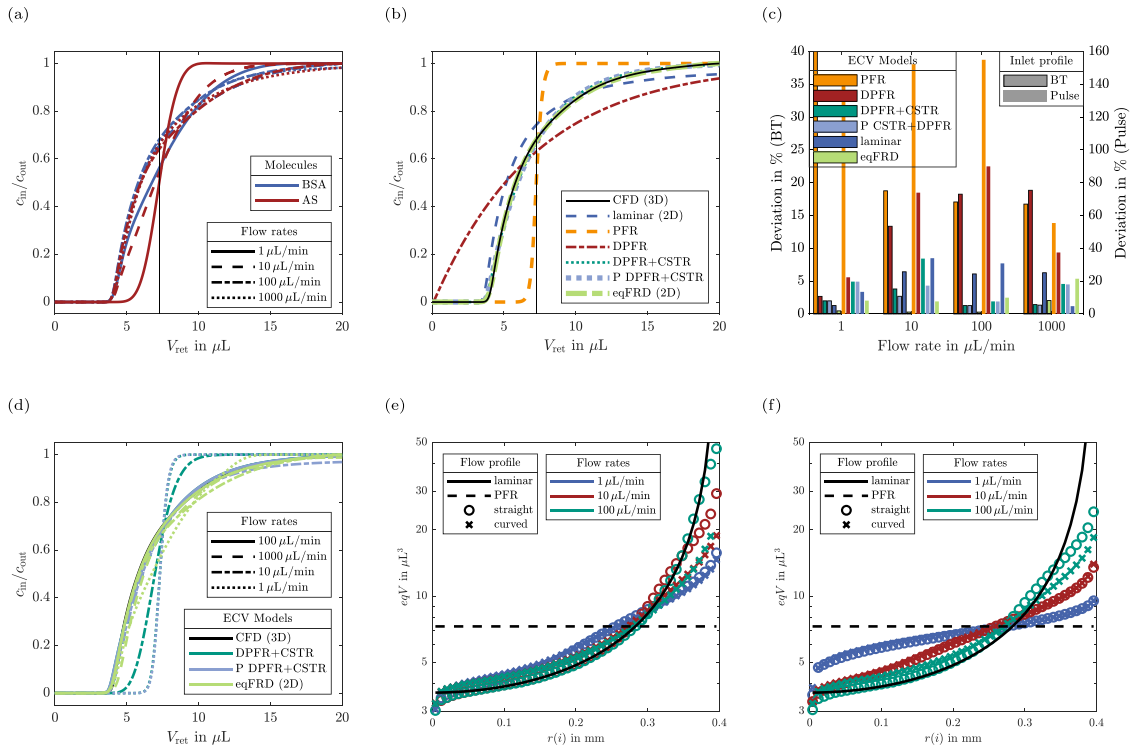

Fig. 5. Modeling of a curved channel with a length of 0.014 m and a diameter of 0.8e−3 m with varying flow rates and different ECV model approaches. The vertical black lines represent the volume of the channel. (a): CFD simulations of a breakthrough at different flow rates for BSA and AS. (b): Breakthrough curve of BSA at a flow rate of 100 μL/min for different modeling approaches. (c): Deviations of different model approaches from the CFD model for breakthrough and pulse injections of BSA. (d): Transfer of fitted ECV models (DPFR+CSTR, P DPFR+CSTR, eqFRD) with parameters $(L, D_{ECV}, s, u(r))$ fitted at various flow rates to a flow rate of 100 μL/min. (e), (f): eqV of BSA (e) and AS (f) at different flow rates for a straight and curved structure in comparison with ideal laminar and PFR behavior.

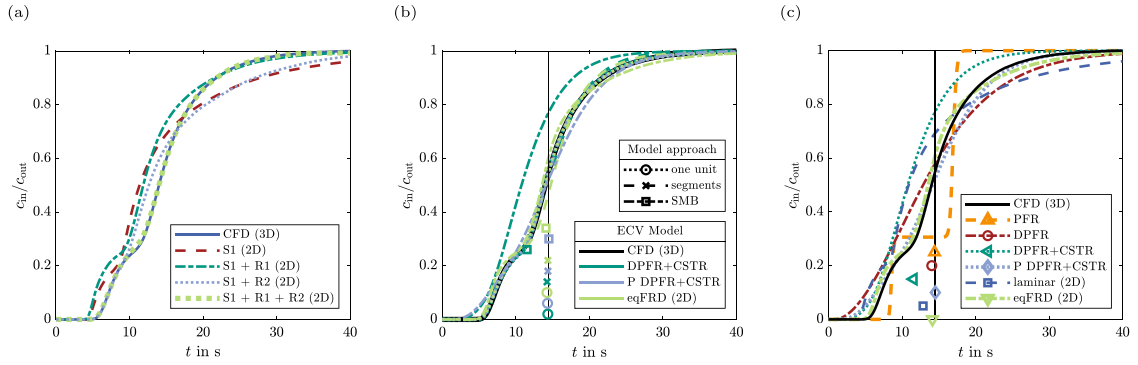

Fig. 6. Modeling of the ECV segment between zone II and zone III. (a): Modeling with the eqFRD approach, using different subsegments of the ECV for the calculation of the model parameters. For explanation of the subsegments, see Fig. 2(b): S1 — Stator 1 & Stator 2; R1 Rotor 1a & Rotor 1b; R2 — Rotor 2a & Rotor 2b. (b): Breakthrough curves (lines) and mean retention times (first moments, markers) for different model approaches. The ECV was either modeled as one unit (according to Fig. 2(c)), as different segments (according to Fig. 2(b)), or in μSMB configuration, where the parameters for all rotating parts were calculated considering the breakthrough curves at all four zone flow rates. (c): Breakthrough curves (lines) and mean retention times (first moments, markers) of the μSMB configuration with different modeling approaches.

As discussed in Section 4.1, subsegments 1, 2, 5, and 6 can be effectively modeled with the laminar approach. This holds true even for the diameter changes between subsegments 1 and 2 and 5 and 6 (results not shown here). In implementation S1, all rotor subsegments were modeled as independent units, as depicted in Fig. 2(b), and the rotor subsegments were modeled with the laminar approach and the stator subsegments with eqFRD, assuming no superimposition of the ECV effects between different subsegments. Subsequently, implementations S1+R1 and S1+R2 combined the stator subsegments with one part of the rotor, using eqFRD to model the combined unit. Finally, in implementation S1+R1+R2, all subsegments along a flow path were combined into one unit, as depicted in Fig. 2(c) and modeled with eqFRD.

The depicted breakthrough curve features a shoulder resulting from the two inlets of the ECV with different retention times. The shoulder represents the breakthrough of molecules entering subsegment 4, while the main breakthrough is from molecules entering subsegment 1. The end concentration of the first breakthrough is much lower due to the lower flow rate entering subsegment 4 (30 vs. 98 μL/min). Only by considering all subsegments of the ECV segment together during model building, the model is able to accurately predict the CFD breakthrough curve, demonstrating that ECV effects are not simply additive in this example. This was to be expected as no radial mixing occurs between the subsegments.

While these results suggest that modeling all subsegments along a flow path as a single unit is the most accurate and simplest approach, it is not always feasible. In the case of the described μSMB

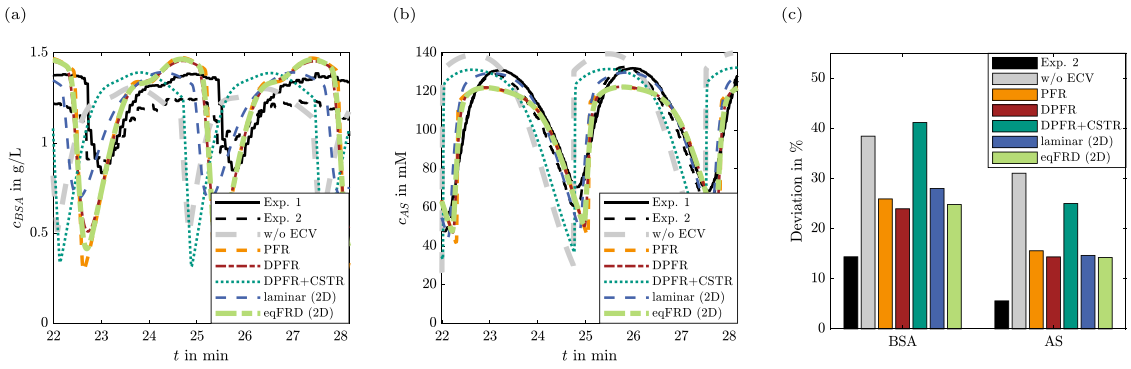

Fig. 7. Comparison of different ECV model approaches for the application of a μSMB system: (a): BSA concentration in the raffinate stream for the first two switches of the third cycle. Simulated concentrations were post-processed with a moving average with a 10 s time interval to match the experimental settings. (b): AS concentration in the extract stream for the first two switches of the third cycle. (c): Deviations of the tested approaches to the experimental results (Exp. 1) over the first three cycles for BSA in the raffinate stream and AS in the extract stream. For better comparability between the molecules, all values were normalized with the over all area of the experimental results.

system, for example, each ECV segment consists of rotating and static parts, resulting in different connections between subsegments in the course of one experiment. Consequently, subsegments must be modeled as separate units to implement these changes in connectivity. This is straightforward for models that do not require parameter fitting, as all subsegments can be modeled independently in accordance with Fig. 2(b). For models requiring parameter fitting, it is crucial to consider the flow through all preceding subsegments, as shown in Fig. 6(a).

In the case of SMB, there is one more point to consider: the rotating parts of the ECV switch between the different zones of the SMB system, hence changing flow rates during an experiment. This can be implemented in models that do not require parameter fitting (at least for the ones considered in this study), as only D_{ECV} changes with flow rate and this can be adjusted in CADET. It is more challenging for fitted models, as the stator model also depends on concentration profiles in the rotor parts. Here, it was investigated whether a model applicable at all required flow rates could be implemented. The resulting breakthrough curves and mean residence times of all the model approaches requiring a parameter fit are depicted in Fig. 6(b).

All model approaches match the CFD breakthrough curve when using a single unit and also when using several units for the subsegments. Only when implementing a model for all flow rates, the DPFR+CSTR approach is not able to predict the breakthrough curve any longer, the deviation is also apparent in the mean retention time. Both, eqFRD and the parallel approach predict the peak shape with high accuracy, though the mean retention time is more accurate with the parallel approach. Still, both approaches seem viable options for modeling the whole segment under varying flow rate conditions.

Fig. 6(c) provides an overview of all model approaches for the entire ECV segment under SMB conditions. The two breakthroughs from the two inlets become more apparent for the PFR approach. The curve is not perfectly rectangular, which shows the impact of numerical dispersion for the chosen discretization. As previously observed, the parallel approach and eqFRD predict the shape of the breakthrough curve with the highest precision, reducing deviations to the CFD model from 8%–11% for all other models to approximately 3%. However, when considering all segments between all the zones, only eqFRD is able to predict the peak shape reliably at all flow rates (compare Fig. S12).

Besides the differences in model complexity and hence computational time, the DPFR and PFR approaches accurately predict the mean retention time as it is not influenced by dispersion. The peak shape, on the other hand, differs significantly. Whether simple 1D models suffice depends on whether peak shape and retention time are crucial or if retention time alone is sufficient. The laminar and DPFR+CSTR approaches underestimate retention time and are unsuitable. For the DPFR+CSTR approach, better model parameters might be found using a different fitting metric, such as considering mean retention time in addition to the mean square error that was applied in this study. The laminar model's shorter retention time results from the not considered dispersion caused by Dean vortices. This effect is compensated in the DPFR model by assuming increased dispersion due to Taylor–Aris dispersion, leading to comparable retention time but differing peak shape.

4.4. Application of ECV models to a μSMB system

Fig. 7 illustrates the application of the developed ECV models to the μSMB system. The experimental data shown are from the triangle theory process point previously published [8], with the experiments performed in duplicate (labeled as Exp. 1 and Exp. 2). Fig. 7(a) displays the first two switches of the third cycle for BSA in the raffinate stream, while Fig. 7(b) shows the same for AS in the extract stream. For comparison, a simulation without any ECV model was also performed. The parallel DPFR+CSTR approach is not depicted due to its disproportionately long computational time.

Both plots show the typical cyclic behavior characteristic of an SMB experiment. When comparing these results to Fig. 6(c), it is evident that all models capable of accurately predicting retention time for the ECV between zones two and three yield comparable results in the μSMB simulation. However, the differences in predicted peak shapes between the various approaches are less pronounced than in the standalone ECV modeling. This is primarily because the column model contributes more significantly to overall dispersion than the ECV. By calculating the first and second moments of the column and ECV outlet profiles, it is estimated that the ECV accounts for 17% of the retention time but only 8% of the peak broadening in the case of BSA. This suggests that for the developed μSMB system, a simple ECV model is sufficient, which is advantageous for scale-up modeling, as those are also state of the art for larger scale SMB system and the same model type can be applied across different scales.

However, especially in the case of BSA, there are noticeable differences between the predicted peak shape and retention time compared to the experimental results for all tested ECV models. Fig. 7(c) provides an overview of the deviations for the first three cycles of the SMB process. Even between the two duplicate experiments, there is a difference of 14% for BSA and 6% for AS. Overall, the deviations are higher for BSA than for AS. For the PFR, DPFR, laminar, and eqFRD models, the deviation is approximately 25% for BSA and 15% for AS. Among the tested models, the laminar model performs slightly better for AS, likely because the experimental conditions are close to the regime where Taylor–Aris dispersion is expected for AS, but not for BSA. The model that disregards the ECV and the DPFR+CSTR model exhibit the highest deviations, underscoring the importance of accounting for

ECV and the challenges in determining suitable model parameters through parameter fitting. These results suggest that all models with calculated parameters would provide a comparable estimation of the SMB process. The influence of the ECV is generally more significant for unretained components [37], as they have a shorter retention time in the column. In this case, both components are unretained, yet their retention times vary significantly. BSA has a pore accessibility of 0, while AS has a pore accessibility of 0.96, resulting in retention volumes of approximately 130 µL and 290 µL, respectively. Consequently, BSA represents the worst-case scenario regarding ECV influence, which also explains the lower deviations observed with AS.

Despite applying the ECV models, significant deviations remain. Possible reasons for these discrepancies include the omission of detector geometry during model parameter determination or effects related to the column model, such as frits or the transition between the column and ECV, both of which have been previously reported to influence detected peaks [21,38]. The frits were included in the column model, and the single-column model was tested across various flow rates. However, these single-column results may not be directly transferable to the μSMB system, as we demonstrated in previous sections that the additivity of the influence of single system components on the outlet profile cannot be assumed. The column endpieces and frits used (fixed endpieces for Omnifit Microbore columns with 2 µm stainless steel frits) have an approximate volume of 18 µL per column. This volume is therefore not negligible compared to the system's ECV, which is approximately 21 µL between columns per zone. Thus, the influence of the endpieces and frits should be examined in greater detail in future studies.

The presented results emphasize the importance of considering ECV in relation to the column itself. The selection of a suitable ECV model should not be based solely on the ECV characteristics but also on the performance of the column and the overall system.

5. Conclusion

In this study, we systematically evaluated various modeling approaches for predicting the effects of extra column volume in a μSMB chromatography system and its ECV entities. Our results highlight that while the laminar model is highly versatile and provides accurate results for straight capillaries across different flow rates, it is less reliable for curved capillaries and channels where Dean vortices are present. In these cases, the here presented eqFRD model offers a viable alternative, particularly for simulations requiring accurate predictions at varying flow rates. When modeling complex ECVs consisting of multiple subsegments, the model accuracy could be increased significantly from approx. 90% with common ECV models to 97% with the parallel DPFR+CSTR and eqFRD approaches. However, the eqFRD model proved more reliable when determining process parameters across several flow rates simultaneously, making it a robust choice for complex systems.

When these approaches were applied to model the entire μSMB system, we found that the choice of ECV model had minimal impact, provided it could accurately predict the retention time within the ECV. This suggests that, in the specific scenario considered, the column plays a much more dominant role in determining peak shape than the ECV, and simpler ECV models may be sufficient to achieve reliable results. Therefore, the selection of an ECV model should always be made in the context of the overall system to avoid unnecessary computational complexity.

For all tested model approaches, there remains a significant deviation between the predicted and experimental results of the μSMB experiments. This indicates that other factors, which were not accounted for in this study, such as the transition between the column and ECV, may need to be considered in future research to further improve model accuracy.

CRediT authorship contribution statement

Juliane Diehm: Writing – original draft, Visualization, Software, Methodology, Investigation, Conceptualization. **Matthias Franzreb:** Writing – review & editing, Conceptualization.

Declaration of competing interest

The authors declare that they have no known competing financial interests or personal relationships that could have appeared to influence the work reported in this paper.

Acknowledgments

J.D. wants to thank the Cusanuswerk e.V. for the funding of her PhD scholarship.

Appendix A. Supplementary data

Supplementary material related to this article can be found online at https://doi.org/10.1016/j.chroma.2024.465543.

Data availability

Data will be made available on request.

References

[1] L. Gerstweiler, J. Bi, A.P.J. Middelberg, Continuous downstream bioprocessing for intensified manufacture of biopharmaceuticals and antibodies, Chem. Eng. Sci. (2020) http://dx.doi.org/10.1016/j.ces.2020.116272.

[2] O. Ötes, H. Flato, J. Winderl, J. Hubbuch, F. Capito, Feasibility of using continuous chromatography in downstream processing: Comparison of costs and product quality for a hybrid process vs. a conventional batch process, J. Biotech. 259 (2017) 213–220, http://dx.doi.org/10.1016/j.jbiotec.2017.07.001, URL https://www.sciencedirect.com/science/article/pii/S0168165617315134.

[3] A. Jungbauer, P. Satzer, A. Duerauer, A. Azevedo, R. Aires-Barros, B. Nilsson, S. Farid, S. Goldrick, M. Ottens, M. Sponchioni, H. Marcelo Fernandez Lahore, Continuous downstream processing, Sep. Purif. Technol. 338 (2024) 126439, http://dx.doi.org/10.1016/j.seppur.2024.126439, URL https://www.sciencedirect.com/science/article/pii/S1383586624001783.

[4] M. Pedeferri, G. Zenoni, M. Mazzotti, M. Morbidelli, Experimental analysis of a chiral separation through simulated moving bed chromatography, Chem. Eng. Sci. 54 (17) (1999) 3735–3748, http://dx.doi.org/10.1016/S0009-2509(99)00031-7, URL https://www.sciencedirect.com/science/article/pii/S0009250999000317.

[5] T.C. Silva, M. Eppink, M. Ottens, Small, smaller, smallest: Miniaturization of chromatographic process development, J. Chromatogr. A 1681 (2022) 463451, http://dx.doi.org/10.1016/j.chroma.2022.463451, URL https://www.sciencedirect.com/science/article/pii/S0021967322006434.

[6] T.C. Silva, M. Eppink, M. Ottens, Automation and miniaturization: Enabling tools for fast, high-throughput process development in integrated continuous biomanufacturing, J. Chem. Technol. Biotechnol. 97 (9) (2022) 2365–2375, http://dx.doi.org/10.1002/jctb.6792, _eprint: https://onlinelibrary.wiley.com/doi/pdf/10.1002/jctb.6792. URL https://onlinelibrary.wiley.com/doi/abs/10.1002/jctb.6792.

[7] C. Kortmann, T. Habib, C. Heuer, D. Solle, J. Bahnemann, A novel 3D-printed and miniaturized periodic counter current chromatography system for continuous purification of monoclonal antibodies, Micromachines 15 (3) (2024) 382, http://dx.doi.org/10.3390/mi15030382, Number: 3 Publisher: Multidisciplinary Digital Publishing Institute. URL https://www.mdpi.com/2072-666X/15/3/382.

[8] J. Diehm, T. Ballweg, M. Franzreb, Development of a 3D printed micro simulated moving bed chromatography system, J. Chromatogr. A 1695 (2023) 463928, http://dx.doi.org/10.1016/j.chroma.2023.463928, URL https://www.sciencedirect.com/science/article/pii/S0021967323001541.

[9] J. Diehm, L. Witting, F. Kirschhöfer, G. Brenner-Weiß, M. Franzreb, Micro simulated moving bed chromatography-mass spectrometry as a continuous online process analytical tool, Anal. Bioanal. Chem. (2023) http://dx.doi.org/10.1007/s00216-023-05023-9, URL https://link.springer.com/10.1007/s00216-023-05023-9.

[10] H. Schmidt-Traub, M. Schulte, A. Seidel-Morgenstern, Preparative Chromatography, second ed., John Wiley & Sons, Ltd, 2012, http://dx.doi.org/10.1002/9783527649280, _eprint: https://onlinelibrary.wiley.com/doi/pdf/10.1002/9783527649280. URL https://onlinelibrary.wiley.com/doi/10.1002/9783527649280.

[11] J.M. Breuer, S. Leweke, J. Schmölder, G. Gassner, E. von Lieres, Spatial discontinuous Galerkin spectral element method for a family of chromatography models in CADET, Comput. Chem. Eng. 177 (2023) 108340, http://dx.doi.org/10.1016/j.compchemeng.2023.108340, URL https://www.sciencedirect.com/science/article/pii/S0098135423002107.

[12] M. Juza, M. Mazzotti, M. Morbidelli, Simulated moving-bed chromatography and its application to chirotechnology, Trends Biotechnol. 18 (3) (2000) 108–118, http://dx.doi.org/10.1016/S0167-7799(99)01419-5, URL https://linkinghub.elsevier.com/retrieve/pii/S0167779999014195.

[13] A. Seidel-Morgenstern, L.C. Keßler, M. Kaspereit, New developments in simulated moving bed chromatography, Chem. Eng. Technol. 31 (6) (2008) 826–837, http://dx.doi.org/10.1002/ceat.200800081.

[14] M. Mazzotti, G. Storti, M. Morbidelli, Optimal operation of simulated moving bed units for nonlinear chromatographic separations, J. Chromatogr. A 769 (1997) 3–24, http://dx.doi.org/10.1016/S0021-9673(97)00048-4.

[15] S. Katsuo, C. Langel, P. Schanen, M. Mazzotti, Extra-column dead volume in simulated moving bed separations: Theory and experiments, J. Chromatogr. A 1216 (7) (2009) 1084–1093, http://dx.doi.org/10.1016/j.chroma.2008.12.031, URL http://www.sciencedirect.com/science/article/pii/S0021967308021961.

[16] C. Migliorini, M. Mazzotti, M. Morbidelli, Simulated moving-bed units with extra-column dead volume, AIChE J. 45 (7) (1999) 1411–1421, http://dx.doi.org/10.1002/aic.690450706, _eprint: https://aiche.onlinelibrary.wiley.com/doi/pdf/10.1002/aic.690450706. URL https://aiche.onlinelibrary.wiley.com/doi/abs/10.1002/aic.690450706.

[17] L.K. Shekhawat, A.S. Rathore, An overview of mechanistic modeling of liquid chromatography, Prep. Biochem. Biotechnol. 49 (6) (2019) 623–638, http://dx.doi.org/10.1080/10826068.2019.1615504, Publisher: Taylor & Francis _eprint: https://doi.org/10.1080/10826068.2019.1615504.

[18] V. Kumar, O. Khanal, M. Jin, Modeling the impact of holdup volume from chromatographic workstations on ion-exchange chromatography, Ind. Eng. Chem. Res. 61 (28) (2022) 10195–10204, http://dx.doi.org/10.1021/acs.iecr.2c01266, Publisher: American Chemical Society.

[19] D. Espinoza, S. Tallvod, N. Andersson, B. Nilsson, Automatic procedure for modelling, calibration, and optimization of a three-component chromatographic separation, J. Chromatogr. A 1720 (2024) 464805, http://dx.doi.org/10.1016/j.chroma.2024.464805, URL https://www.sciencedirect.com/science/article/pii/S002196732400178X.

[20] K. Baran, W.K. Marek, W. Piatkowski, D. Antos, Effect of flow behavior in extra-column volumes on the retention pattern of proteins in a small column, J. Chromatogr. A 1598 (2019) 154–162, http://dx.doi.org/10.1016/j.chroma.2019.03.060, URL https://www.sciencedirect.com/science/article/pii/S0021967319303280.

[21] B. Filip, R. Bochenek, K. Baran, D. Strzałka, D. Antos, Influence of the geometry of extra column volumes on band broadening in a chromatographic system. Predictions by computational fluid dynamics, J. Chromatogr. A 1653 (2021) 462410, http://dx.doi.org/10.1016/j.chroma.2021.462410, URL https://www.sciencedirect.com/science/article/pii/S0021967321005343.

[22] D. Iurashev, S. Schweiger, A. Jungbauer, J. Zanghellini, Dissecting peak broadening in chromatography columns under non-binding conditions, J. Chromatogr. A 1599 (2019) 55–65, http://dx.doi.org/10.1016/j.chroma.2019.03.065, URL https://www.sciencedirect.com/science/article/pii/S0021967319303498.

[23] E. von Lieres, J. Wang, M. Ulbricht, Model based quantification of internal flow distributions from breakthrough curves of flat sheet membrane chromatography modules, Chem. Eng. Technol. 33 (6) (2010) 960–968, http://dx.doi.org/10.1002/ceat.200900614, _eprint: https://onlinelibrary.wiley.com/doi/pdf/10.1002/ceat.200900614. URL https://onlinelibrary.wiley.com/doi/abs/10.1002/ceat.200900614.

[24] Y. Qu, I. Baker, J. Black, L. Fabri, S.L. Gras, A.M. Lenhoff, S.E. Kentish, Application of mechanistic modelling in membrane and fiber chromatography for purification of biotherapeutics — A review, J. Chromatogr. A 1716 (2024) 464588, http://dx.doi.org/10.1016/j.chroma.2023.464588, URL https://www.sciencedirect.com/science/article/pii/S0021967323008130.

[25] G.I. Taylor, Dispersion of soluble matter in solvent flowing slowly through a tube, Proc. R. Soc. A 219 (1137) (1953) 186–203, http://dx.doi.org/10.1098/rspa.1953.0139, URL https://royalsocietypublishing.org/doi/10.1098/rspa.1953.0139.

[26] R. Aris, G.I. Taylor, On the dispersion of a solute in a fluid flowing through a tube, Proc. R. Soc. A 235 (1200) (1997) 67–77, http://dx.doi.org/10.1098/rspa.1956.0065, Publisher: Royal Society. URL https://royalsocietypublishing.org/doi/10.1098/rspa.1956.0065.

[27] A. Shankar, A.M. Lenhoff, Dispersion in round tubes and its implications for extracolumn dispersion, J. Chromatogr. A 556 (1) (1991) 235–248, http://dx.doi.org/10.1016/S0021-9673(01)96224-7, URL https://www.sciencedirect.com/science/article/pii/S0021967301962247.

[28] W.R. Dean, Note on the motion of fluid in a curved pipe, Lond. Edinb. Dublin Philos. Mag. J. Sci. 4 (20) (1927) 208–223, http://dx.doi.org/10.1080/14786440708564324, Publisher: Taylor & Francis _eprint: https://doi.org/10.1080/14786440708564324.

[29] J. Beck, W. Heymann, E. von Lieres, R. Hahn, Compartment model of mixing in a bubble trap and its impact on chromatographic separations, Processes 8 (7) (2020) 780, http://dx.doi.org/10.3390/pr8070780, Number: 7 Publisher: Multidisciplinary Digital Publishing Institute. URL https://www.mdpi.com/2227-9717/8/7/780.

[30] J. Diehm, V. Hackert, M. Franzreb, Configurable 3D printed microfluidic multiport valves with axial compression, Micromachines 12 (10) (2021) 1247, http://dx.doi.org/10.3390/mi12101247, URL https://www.mdpi.com/2072-666X/12/10/1247.

[31] A. Polson, Some aspects of diffusion in solution and a definition of a colloidal particle, J. Phys. Colloid Chem. 54 (5) (1950) 649–652, http://dx.doi.org/10.1021/j150479a007, URL https://pubs.acs.org/doi/abs/10.1021/j150479a007.

[32] J.G. Albright, J.P. Mitchell, D.G. Miller, Interdiffusion coefficients, densities, and refractive indices of ammonium chloride + water and ammonium sulfate + water at 25.degree.C, J. Chem. Eng. Data 39 (1) (1994) 195–200, http://dx.doi.org/10.1021/je00013a055, URL https://pubs.acs.org/doi/abs/10.1021/je00013a055.

[33] R. Mohan, O. Kaytancioglu, A.S. Myerson, Diffusion and cluster formation in supersaturated solutions of ammonium sulfate at 298K, J. Cryst. Growth 217 (4) (2000) 393–403, http://dx.doi.org/10.1016/S0022-0248(00)00528-5, URL https://www.sciencedirect.com/science/article/pii/S0022024800005285.

[34] S. Leweke, E. von Lieres, Chromatography analysis and design toolkit (CADET), Comput. Chem. Eng. 113 (2018) 274–294, http://dx.doi.org/10.1016/j.compchemeng.2018.02.025, URL https://www.sciencedirect.com/science/article/pii/S0098135418300966.

[35] J.G. Atwood, M.J.E. Golay, Dispersion of peaks by short straight open tubes in liquid chromatography systems, J. Chromatogr. A 218 (1981) 97–122, http://dx.doi.org/10.1016/S0021-9673(00)82050-6, URL https://www.sciencedirect.com/science/article/pii/S0021967300820506.

[36] G. Desmet, K. Broeckhoven, Extra-column band broadening effects in contemporary liquid chromatography: Causes and solutions, TRAC Trends Anal. Chem. 119 (2019) 115619, http://dx.doi.org/10.1016/j.trac.2019.115619, URL https://linkinghub.elsevier.com/retrieve/pii/S016599361930353X.

[37] F. Gritti, A. Felinger, G. Guiochon, Influence of the errors made in the measurement of the extra-column volume on the accuracies of estimates of the column efficiency and the mass transfer kinetics parameters, J. Chromatogr. A 1136 (1) (2006) 57–72, http://dx.doi.org/10.1016/j.chroma.2006.09.074, URL https://linkinghub.elsevier.com/retrieve/pii/S0021967306018267.

[38] S. Schweiger, A. Jungbauer, Scalability of pre-packed preparative chromatography columns with different diameters and lengths taking into account extra column effects, J. Chromatogr. A 1537 (2018) 66–74, http://dx.doi.org/10.1016/j.chroma.2018.01.022, URL https://www.sciencedirect.com/science/article/pii/S0021967318300189.